Superconducting YBa$_2$Cu$_3$O$_{7-\delta}$ Nanocomposites Using Preformed ZrO$_2$ Nanocrystals: Growth Mechanisms and Vortex Pinning Properties

Katrien De Keukeleere, Pablo Cayado, Alexander Meledin, Ferran Vallès, Jonathan De Roo, Hannes Rijckaert, Glenn Pollefeyt, Els Bruneel, Anna Palau, Mariona Coll, Susagna Ricart, Gustaaf Van Tendeloo, Teresa Puig, Xavier Obradors,* and Isabel Van Driessche*

ABSTRACT

Although high temperature superconductors are promising for power applications, the production of low-cost coated conductors with high current densities—at high magnetic fields—remains challenging. A superior super-conducting YBa$_2$Cu$_3$O$_{7-\delta}$ nanocomposite is fabricated via chemical solution deposition (CSD) using preformed nanocrystals (NCs). Preformed, colloidally stable ZrO$_2$ NCs are added to the trifluoroacetic acid based precursor solution and the NCs' stability is confirmed up to 50 mol% for at least 2.5 months. These NCs tend to disrupt the epitaxial growth of YBa$_2$Cu$_3$O$_{7-\delta}$, unless a thin seed layer is applied. A 10 mol% ZrO$_2$ NC addition proved to be optimal, yielding a critical current density J_C of 5 MA cm^{-2} at 77 K in self-field. Impor-tantly,this new approach results in a smaller magnetic field decay of J_C(H//c) for the nanocomposite compared to a pristine film. Furthermore, microstruc-tural analysis of the YBa$_2$Cu$_3$O$_{7-\delta}$ nanocomposite films reveals that different strain generation mechanisms may occur compared to the spontaneous segregation approach. Yet, the generated nanostrain in the YBa$_2$Cu$_3$O$_{7-\delta}$ nanocomposite results in an improvement of the superconducting properties similar to the spontaneous segregation approach. This new approach, using preformed NCs in CSD coatings, can be of great potential for high magnetic field applications.

1. Introduction

Since the discovery of high-temperature superconductors (HTS), huge efforts have been dedicated to develop useful conduc-tors for, e.g., power applications.[1] In this respect, low fabrication costs and high crit-ical current densities in a magnetic field are required. Chemical solution deposition (CSD) is an appealing method toward the production of affordable, long length HTS tapes.[2] In this method, a precursor solu-tion containing the metal salts is deposited on a metallic substrate (or single crystal on lab scale) and thermally treated to obtain the desired superconducting film. In particular, methanol-based solutions containing the trifluoroacetate salts of YBa$_2$Cu$_3$O$_{7-\delta}$ (YBCO) have been reported to yield epitaxial layers with high critical current densities (J_C = 2–4 MA cm^{-2}).[3] However, these epitaxial YBCO films still feature a strong J_C reduction with increasing magnetic fields, revealing new challenges for high field applications.[4] Magnetic flux quanta, i.e., vortices, appear

in a superconducting film upon applying a magnetic field. These vortices move throughout the superconductor under the influence of a Lorentz force, causing a reduction in J_C. Vortices can be immobilized, or pinned, by the introduction of nonsu-perconducting defects of the size of the vortex core, i.e., a few nm. These so-called artificial pinning centers (APCs) can effec-tively decrease the magnetic field dependence of J_C.[1a,5]

To date, outstanding performances of CSD-based YBCO films are obtained under a high magnetic field through the introduc-tion of secondary nanometric phases in the YBCO matrix. In this case, extra metal salts are added to the YBCO precursor solution to grow the desired secondary phase (e.g., Au, Y$_2$O$_3$, BaZrO$_3$, BaCeO$_3$, Ba$_2$YTaO$_6$) via spontaneous segregation during the YBCO growth.[5a,6] Although this method yields effective, nanostructured superconducting layers, some limi-tations remain. Since this method relies on the spontaneous segregation of secondary phases, limited control over the nano-particles' formation is obtained and, as a consequence, the size, and size distribution of the particles remains challenging.

A more interesting approach to improve the CSD-based YBCO films is the addition of preformed nanocrystals (PNCs) to the YBCO precursor solution. This approach should offer a better control of the APC size. Here, nonaqueous synthesis methods, being surfactant-assisted or surfactant-free, can be used yielding monodisperse nanocrystals with different sizes and shapes.[7] So far, only a few reports using preformed pinning centers have been reported in literature.[6f,8] The first account was disclosed by Martinez-Julien et al. in 2011, who used preformed Au nanocrystals (NCs).[6f] In this approach, only a low amount of Au NCs (up to 2 mol%) could be stabi-lized in the YBCO precursor. Unfortunately, the Au NCs were pushed to the YBCO surface during the treatment, unable to enhance vortex pinning. Bretos et al. described the introduc-tion of amorphous $BaZrO_3$ nanoparticles in YBCO.[8a] Yet, the improvement in critical current of the YBCO films was rather ascribed to an improved surface morphology of the sample than to the improvement of flux pinning provided by the $BaZrO_3$ nanoparticles. More recently, we described the intro-duction of preformed CeO_2 and ZrO_2 NCs to the YBCO film.[8b] The CeO_2 NCs remain stable in the YBCO precursor up to a week at desirable concentrations (up to 32 mol%). Interestingly, a difference in NC size (2 nm vs 6 nm) appeared to have an effect on the NC mobility during the thermal processing. The smaller NCs migrated to the film surface, while the larger ones were retained in the film itself. However, the J_c field depend-ence of the YBCO nanocomposite did not exceed the one of pristine YBCO. Preliminary results using preformed ZrO_2 NCs indicated that the PNCs settle at the substrate–YBCO interface, leading to poorly grown YBCO and deteriorating supercon-ducting properties.[8b] However, the introduction of an inter-facial YBCO seed layer between the substrate and the YBCO nanocomposite can promote epitaxial YBCO growth.[6h,8b,9]

In this work, a comprehensive study was performed on the involved phenomena of the ZrO_2 NCs' settling on the sub-strate and an in-depth study of the influence of the use of a pure YBCO seed layer. First, the ZrO_2 NCs are synthesized via a microwave-assisted solvothermal treatment, yielding aggregated NCs of 7 nm directly after synthesis.[10] Through a post-synthetic surface treatment with hydrophobic ligands, the NCs become aggregate-free and are colloidally stable in apolar solvents. However, as the methanol-based YBCO precursor solution provides a polar environment, a ligand exchange is mandatory. This is not always straightforward, as the surface chemistry of metal oxide NCs is more complex compared to the surface chemistry of the more established chalcogenides.[11] The ZrO_2 PNCs can be stabilized in high concentration, up to 50 mol%, for at least 2.5 months in a trifluoroacetic acid (TFA) YBCO precursor solution, by using the combination of a strong organic acid and an amino acid,[12] confirmed by dynamic light scattering analysis. Second, the YBCO-PNCs suspensions were deposited on a $LaAlO_3$ (LAO) substrate through spin coating and subsequently treated at high temperatures to study the influence of the PNCs on the superconducting performances and the microstructure of the grown YBCO nanocomposite film. X-ray photoelectron spectroscopy (XPS) analysis and quench studies revealed that the PNCs already settle at the substrate interface during pyrolysis, before the YBCO growth. The use of a pure YBCO seed layer, on the other hand, indeed resulted in desirable YBCO growth. Here, an in-depth study on the superconducting and microstructural properties was con-ducted. An optimal critical current density J_c of 5 MA cm^{-2}, an improved magnetic field dependency of J_c and an effec-tive pinning behavior at elevated magnetic fields was found for the 10 mol% PNC addition compared to pristine YBCO. Microstructural analysis revealed that the PNC-YBCO nano-composites show a modified nanostrain distribution, compared to the spontaneous segregation approach, although a similar nanostrain value was found. Moreover, the angular dependency and irreversibility line measurements showed that the vortex pinning properties encountered in the PNC-YBCO nanocom-posites have a similar origin than the ones reported for sponta-neously segregated NCs.

2. Results and Discussion

2.1. Nanocrystal Stabilization

ZrO_2 NCs were synthesized via a microwave-assisted method, and have the monoclinic crystal structure according to X-ray dif-fraction (XRD) (**Figure 1**B). Transmission electron microscope (TEM) analysis on the NCs after surface modification shows individual NCs with a long edge of about 7 nm (Figure 1A). Dynamic light scattering (DLS) analysis confirms the presence of individual, aggregate-free NCs in chloroform with an average solvodynamic diameter of 10 nm. As the solvodynamic diam-eter is defined as the sum of core and

ligand in apolar solvents, the obtained value is in agreement with the size determined by TEM (Figure 1C). The transfer from chloroform to methanol with glutamine (Gln) and trifluoroacetic anhydride leads to a similar size distribution in DLS (Figure 1C) confirming the suc-cess of the stabilization. In order to apply these NCs as pinning centers in superconductors, it is essential that the NCs remain stable in the highly ionic TFA-YBCO precursor solution. Dif-ferent NC concentrations capped with Gln were introduced in a 0.75 M (total metal concentration) TFA-YBCO solution. DLS analyses on these suspensions show that even at high loadings, the colloidal integrity is maintained in this ionic environment (Figure 1C). Moreover, these suspensions remain stable for at least 2.5 months, sufficient for usage as nanocomposite precur-sors. For the 50 mol% NCs-YBCO suspension, some agglom-eration starts to occur after four months, see Figure S1 in the Supporting Information.

2.2. Layer Formation

Preliminary results using preformed ZrO_2 NCs showed that high PNC loadings resulted in random and thus poorly grown YBCO, whereas the self-field J_C value and the magnetic field dependence of J_C at lower amounts did not increase signifi-cantly compared to the pristine YBCO layer.[8b] Moreover, the initial ZrO_2 PNCs transformed to $BaZrO_3$ NCs during the crystallization treatment (see Figures S2–S4 and Table S1, Sup-porting Information).[8b] To assess when the PNCs settle at the substrate—during deposition, pyrolysis or crystallization— we performed a centrifugation experiment and XPS analyses,
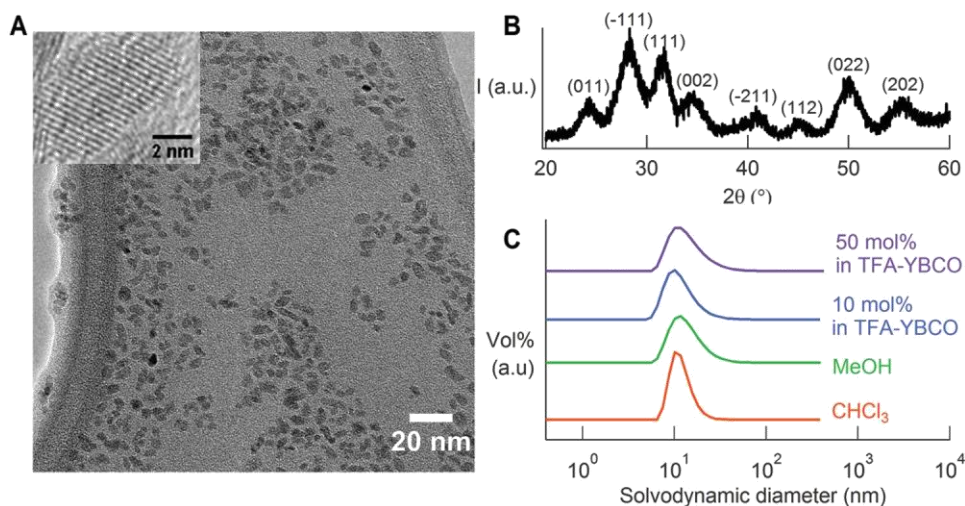

Figure 1. A) Bright fi eld and high resolution TEM and B) XRD analysis of the monoclinic ZrO_2 NCs after synthesis and post-modifi cation in chloroform. C) DLS analysis of the ZrO_2 NCs in chloroform, methanol, and 10 and 50 mol% in TFA-YBCO precursor solution.

revealing that the ZrO_2 PNCs settle on the substrate during the pyrolysis treatment (see Figures S5 and S6A,B, Supporting Information). The crystallization of ZrO_2 to $BaZrO_3$ occurs through the reaction with the BaF_2 phase, present during the thermal treatment. However, also YBCO nuclei are formed through the reaction with BaF_2, controlled by the wet atmos-phere.[13] This means that competition between the crystal-lization kinetics of $BaZrO_3$ and YBCO nuclei formation takes place at the interface, as a Zr-rich phase is already present at the interface after pyrolysis. Hence, the balance between the heterogeneous nucleation rates of $BaZrO_3$ and YBCO will determine the final concentration of the $BaZrO_3$ NCs at the interface. XRD experiments performed on quenched samples of the YBCO nanocomposite layers indicate that $BaZrO_3$, origi-nating from the ZrO_2 PNCs, nucleates before YBCO formation (see Figure S7, Supporting Information). This means that the $BaZrO_3$ NCs are formed first at the interface through heteroge-neous nucleation. As the lattice mismatch between $BaZrO_3$ and YBCO is fairly high (i.e., 8%), random (103) YBCO is formed when high amounts of the preformed ZrO_2 NCs are added. However, the YBCO homoepitaxial nucleation rate will always

be higher than the heteroepitaxial one.[14] This means that the use of an YBCO seed layer will promote a faster formation of YBCO nuclei and a reduced concentration of BaZrO$_3$ NCs at the interface, resulting in an improved epitaxial quality of the YBCO nanocomposite.

In order to promote *c*-axis oriented YBCO growth, we deposited a 50–60 nm pure YBCO seed layer in between the LAO substrate and the YBCO nanocomposite film. Nanocomposite films with different PNCs' amounts were tested, i.e., 0, 3, 6, 10, and 15 mol% of preformed ZrO$_2$ NCs, deposited onto the YBCO seed layer. According to the XRD diffraction patterns displayed in **Figure 2**, all the nanocomposite films are *c*-axis oriented. The PNCs-YBCO nanocomposites show an additional 2ϑ reflection at 43° of (*200*) BaZrO$_3$ (BZO), and the 15 mol% ZrO$_2$ NC addition reveals an extra reflection at 30° of (*110*) BaZrO$_3$, while ZrO$_2$ reflections remain absent. This suggests the complete transformation of the initial ZrO$_2$ NCs into BaZrO$_3$ NCs during the heat treatment. All 2D X-ray diffraction patterns of the films containing PNCs show epitaxial YBCO, while polycrystalline or random YBCO is absent. So indeed, the presence of an interfacial YBCO layer has a beneficial effect on the PNCs-YBCO epitaxial growth.
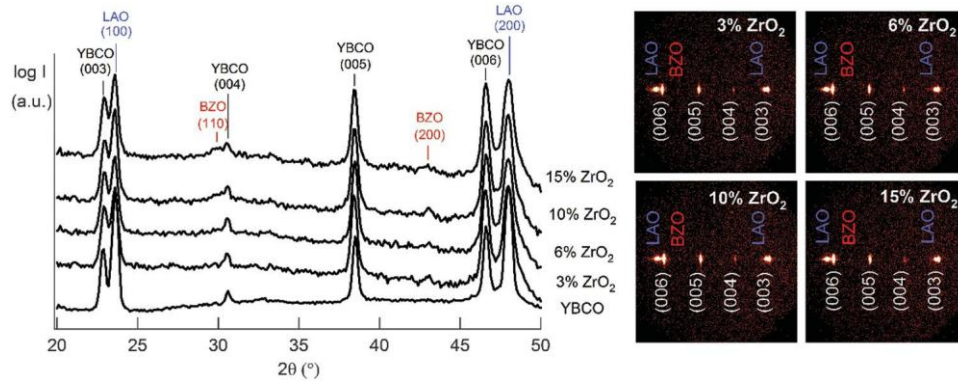

Figure 2. (2D-) XRD diffraction patterns of YBCO fi lms with 0, 3, 6, 10, and 15 mol% of preformed ZrO$_2$ NCs deposited on a LAO substrate with a 50 nm pure YBCO seed layer
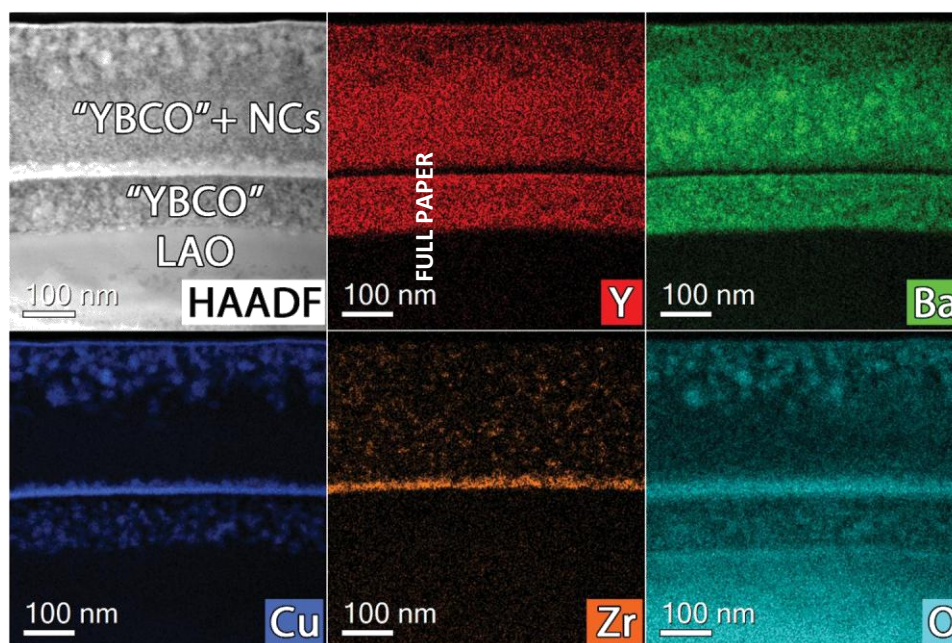
Figure 3. HAADF-STEM cross sectional image and EDX mapping of Y, Ba, Cu, Zr, and O obtained after the pyrolysis treatment of a 15 mol% PNCs-YBCO nanocomposite containing a pure YBCO seed layer.

The YBCO nanocomposite films were investigated both after the pyrolysis and the crystallization treatment via high-angle annular dark field scanning transmission electron microscopy (HAADF-STEM) and energy dispersive X-ray spectroscopy (EDX) analysis (**Figures 3** and **4**). The HAADF image, together with the elemental distribution of the pyrolyzed nanocom-posite, i.e., after the YBCO metal organic decomposition pro-cess, is displayed in Figure 3. The HAADF image reflects the typical porous structure of YBCO films after pyrolysis,[3] though the EDX images clearly show a Zr and Cu aggregation at the interface. From this, it can be concluded that a Zr-rich phase is accumulated at the interface of both YBCO layers. Note that the initial ZrO_2 NCs are not diffusing into the YBCO seed layer. The Cu enrichment is actually a CuO phase (generally CuO nanoparticles with a diameter of 10 nm), typically formed after the pyrolysis treatment from Cu-TFA.[2b] So, it seems that the CuO phase behaves as a very efficient diffusion barrier for the preformed ZrO_2 NCs. The formation of the enriched CuO layers at the interface of pyrolyzed films of TFA-YBCO precursors, after a multideposition process, has been previously reported.[5b] There, it was shown that these enriched CuO layers did not preclude the achievement of homogeneous YBCO films after crystallization. TEM and EDX images of the crystallized nanocomposite are presented in Figure 4. Here, it is clear that the bottom 50–70 nm of the YBCO layer does not contain a Zr-rich phase, while the formed $BaZrO_3$ NCs are more homoge-neously distributed in the top YBCO layer (Figure 4A,B). The individual NCs embedded in the layer coarsen from the initial 7 nm ZrO_2 NCs to 12–25 nm $BaZrO_3$ NCs (Figure 4C), similar to the case of "in-situ" nanocomposites. Some agglomeration of different initial NCs is also clearly visible (Figure 4D). This agglomeration may already occur during the pyrolysis step, but it may also be induced during the crystallization process as a consequence of grain coalescence,[14b] a phenomenon also observed in "in situ" nanocomposites.[15] XPS analysis on both the pyrolyzed and crystallized nanocomposite layer confirms that a Zr-rich phase is only present in the upper YBCO layer and not in the YBCO seed layer (see Figure S6C,D, Supporting
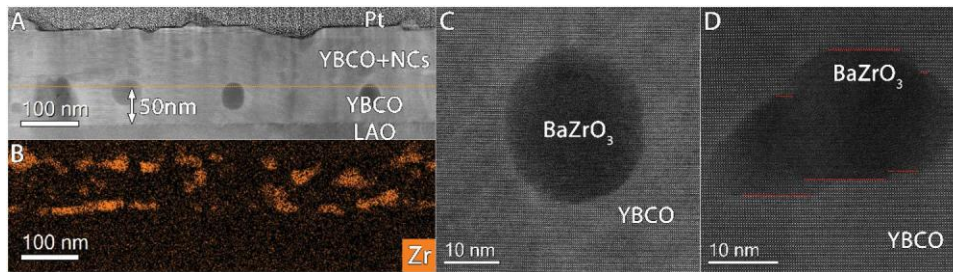
Figure 4. A) HAADF-STEM cross sectional image and B) EDX Zr maping after the pyrolysis and crystallization treatment of a 10 mol% preformed PNCs-YBCO nanocomposite indicating the presence of Zr in the layer. C,D) High-resolution HAADF-STEM Z-contrast image of the same nanocomposite showing $BaZrO_3$ NCs randomly oriented and sometimes faceted by the YBCO (*001*) plane (marked by the red dot lines).
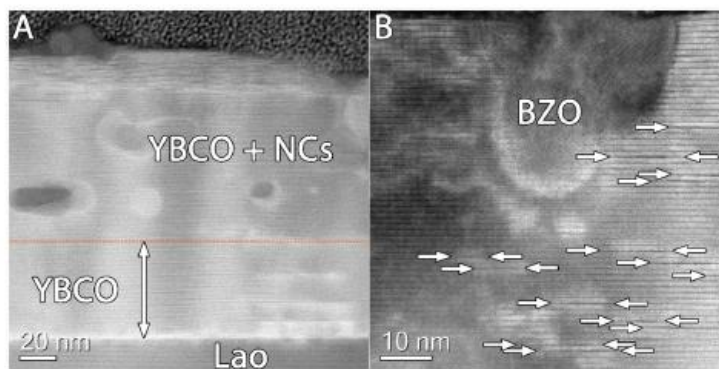

Figure 5. A) LAADF-STEM cross sectional image showing the nanocrystal distribution and the presence of CuO stacking faults in the 10 mol% PNCs–YBCO nanocomposite. B) High-resolution LAADF-STEM image of the same nanocomposite showing the presence of $BaZrO_3$ NCs, indicating highly strained $BaZrO_3$/YBCO interfaces (bright contrast) and short CuO stacking faults (indicated by white arrows).

Information). The XPS analysis also reveals that some enrichment of ZrO_2 NCs occurs at the interface, from which the effect is more prominent after the pyrolysis step than after the crystallization, as confirmed by HAADFSTEM and EDX analysis. So, although an accumulation tendency of the ZrO_2 NCs at the substrate interface exist during the pyrolysis, the use of a pyrolyzed YBCO seed layer with a reduced porosity clearly hinders the diffusion of the PNCs to the LAO interface, and thus influences the YBCO epitaxial film nucleation process as homo-nucleation is now promoted. Another remarkable feature of the present YBCO nanocomposites, using PNCs, concerns the issue of the defect structure induced by the NCs. As commonly seen in nanocomposites formed via the spontaneous segregation approach, the introduction of nanosized secondary phases induces stacking faults (double or triple CuO chain layers) and hereby leads to a heavily strained YBCO matrix at the nanoscale. It has been proposed that this nanostrain can be correlated to the effective pinning properties and it is therefore believed to be essential in order to obtain enhanced self-field J_C values and a smaller magnetic field decay of J_C (H//c). [6d, 7b,10] To determine when $BaZrO_3$, originating from the ZrO_2 PNCs, nucleates during the crystallization treatment, quench experiments were performed on PNC-YBCO layers at different temperatures during the heating ramp. According to XRD experiments performed on these quenched samples (see Figure S7, Supporting Information), it is very likely that the homogeneously nucleated $BaZrO_3$ NCs, originating from the ZrO_2 PNCs, are formed before the full YBCO film is grown, similar to the nanocomposites obtained via spontaneous segregation. Moreover, the $BaZrO_3$ nanocrystals are not biaxially textured within the matrix, comparable to the spontaneous segregation approach, which mostly leads to the formation of incoherent interfaces. However, as seen in the high resolution HAADF-STEM images in Figure 4 , the incorporation of $BaZrO_3$ nanocrystals in the YBCO matrix is also possible without the formation of these stacking faults. Yet, the YBCO surrounding the nanocrystals is clearly strained around the nanocrystal–YBCO interface, as illustrated by the bright contrast surrounding the nanocrystals in the low-angle annular dark field scanning transmission electron microscopy (LAADF-STEM) images given in Figure 5 . In other regions though, short stacking faults in close proximity of the $BaZrO_3$ nanocrystals are observed, as specified by the white arrows in Figure 5 B. This indicates that several sources exist which lead to heavily strained nanoscale regions. The kinetics, involved in the growth process, is influenced by the crystallization of the $BaZrO_3$ NCs. In the present case, a topotactic reaction of ZrO_2 with Ba^{2+} ions occurs, which may lead to a modified strain generation mechanism, affecting the overall microstructure. In the spontaneous segregation approach, on the other hand, the crystallized $BaZrO_3$ NCs are nucleated and grown under the same conditions as YBCO. [5a] As also observed in the spontaneous segregated approach, [6h] it is noticeable that some of the $BaZrO_3$ NCs embedded in the YBCO matrix display facets parallel to CuO_2 planes of YBCO (Figure 4 D), probably indicating that a dense plane is formed and hence the NCs have some local uniaxial texture. Additionally, the known incorporation of small amounts of Y^{3+} into the $BaZrO_3$ crystal structure will also follow a topotactic reaction, thus possibly inducing additional structural or chemical changes at the NC's interface. The modified reaction path interface structure emanating from this new approach can certainly cause a modified growth process of the YBCO nanocomposite films, which can lead to a modified nanostrain distribution, including heavily strained interfaces as shown in Figure 5 B. We should note that the final values of YBCO films nanostrain, as determined through X-ray diffraction, appear similar in both cases reaching a maximum nanostrain ε of 0.24% for the 10 mol% NC in comparison with a nanostrain ε of 0.1% for the pristine sample. [6h,16]

2.3. Superconducting Properties

The investigation of the superconducting properties demonstrated the success of our PNC approach to enhance vortex pinning. Figure 6 A represents the magnetic field dependence of the transport critical current, J_C (H//c), at 77 K for the 6,
10, and 15 mol% ZrO_2 nanocomposites and a pristine YBCO film, determined via transport measurements. All the samples
show high self-field critical current densities, from J_C sf ≈ 2 to 5 MA cm $^{-2}$. In the case of the nanocomposite with 15 mol% ZrO_2 , the reduction of J_C sf could be ascribed to a reduction of the effective cross section due

to a plausible agglomeration of NCs, as observed in CSD nanocomposites for high nanoparticles concentrations. [6a] For the 10 mol% ZrO$_2$ nanocomposite, an overall increase of J C occurs at 77 K up to 5 T, whereas above this 5 T, J C decreases below the pristine fi lm suggesting a decrease of the irreversibility line (IL) (vide infra). Overall, we observe a smaller magnetic fi eld decay of J C (H) for all nanocomposites marked with an extended J C (H) plateau, i.e., a shift of H* to higher fi elds from 0.04 to 0.15 T (see Figure 6 A inset).
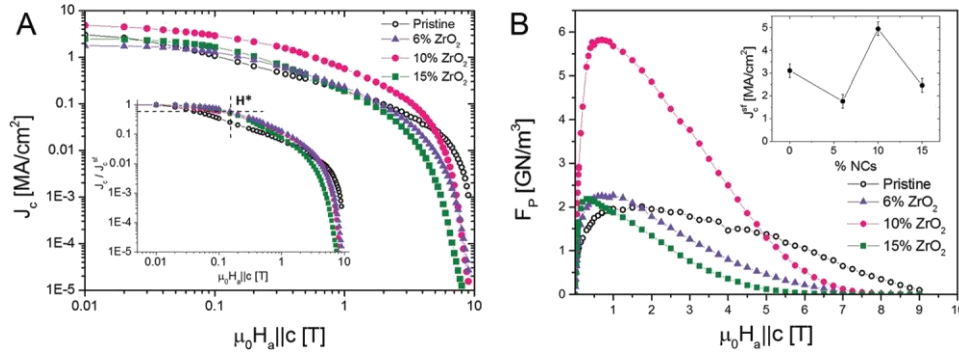

Figure 6. A) Critical current density versus magnetic fi eld at 77 K for YBCO samples with different NC content and a pristine fi lm, determined via transport measurements. The inset shows the same curves normalized to J_C^{sf}, where the H* value ($J_C(H^*) = 0.6\, J_C^{sf}$) obtained for the nanocomposites is indicated. B) Magnetic fi eld dependence of the pinning force at 77 K for a pristine YBCO fi lm and YBCO nanocomposite fi lms containing different NC amounts. The inset shows the J_C^{sf} values for the various PNC concentrations.

H* is the crossover magnetic field from a single vortex pinning to a vortex–vortex collective pinning regime. So, the H* shift confirms that the amount of artificial pinning center sites has strongly increased in all nanocomposites.

The addition of PNCs do not decrease the critical tempera-ture T_C, although the transition width (T) rises drastically to 5.4 K when 15 mol% PNCs are added to the YBCO layer in com-parison with the T = 1.5 K of the 6 mol% NC, again implying that a higher mol% leads to a degradation of the supercon-ductor. Figure 6B shows the pinning force, F_p, as a function of magnetic field for the three nanocomposites in comparison with the pristine film. Notice that F_p increases up to 6 GN m^{-3} for the 10 mol% ZrO$_2$, being three times larger than the pris-tine film, although a clear enhancement is not observed for the other two nanocomposites. This clearly confirms that an optimum amount of NCs exists for this growth process which is around 10 mol% PNC. This value is still lower than the best values reported from BaZrO$_3$ NCs formed via spontaneous seg-regation (10–22 GN m^{-3}),[5a] which encourages us that further optimization is possible in this new approach. We also notice that the maximum pinning force is reached at lower magnetic fields ($\approx$0.5 T–0.8 T) in all the nanocomposites compared to the pristine sample, again probably as a consequence of their lower IL. Therefore, we envisage that much higher pinning forces could be obtained upon optimization of the IL.

From the angular dependence transport critical current measurements (**Figure 7**A), we observe a similar behavior as for the spontaneous segregated nanocomposite approach. The broadening of the peak at H//ab (ϑ = 90°) is typically attributed to the effective pinning of the stacking faults present in the CSD nanocomposite.[17] Additionally, the peak at H//c, is clearly reduced for the nanocomposite. This peak is typically correlated to twin boundary pinning. As this peak can be observed in the pristine YBCO film, the reduction in the nanocomposite indi-cates a loss of the twin boundary coherence along the c-axis, as previously reported.[18] Clearly, the J_C(H//ab) peak is much wider for the 10 mol% ZrO$_2$ nanocomposite film compared to the pristine film at all magnetic fields (see Figure 7 at 65 K). The determination of the FWHM of this peak, ϑ, for all nano-composites at 1 T, 5 T, and 9 T at 65 K is shown in Figure 7B. This clearly confirms that the ab peak broadens in all the nano-composites, while a maximum effect for the one with 10 mol% ZrO$_2$ NC

addition is observed. This demonstrates the effective stacking fault pinning in all the nanocomposites with max-imum effectiveness for samples with 10 mol% NCs.

Finally, **Figure 8**A shows the IL for a pristine YBCO film compared to YBCO nanocomposites films. Here, we confirm that the nanocomposites show a lower IL, which we ascribe to a lower *c*-axis correlation of twin boundaries due to the pres-ence of stacking faults.[18] This reduction is more evident in
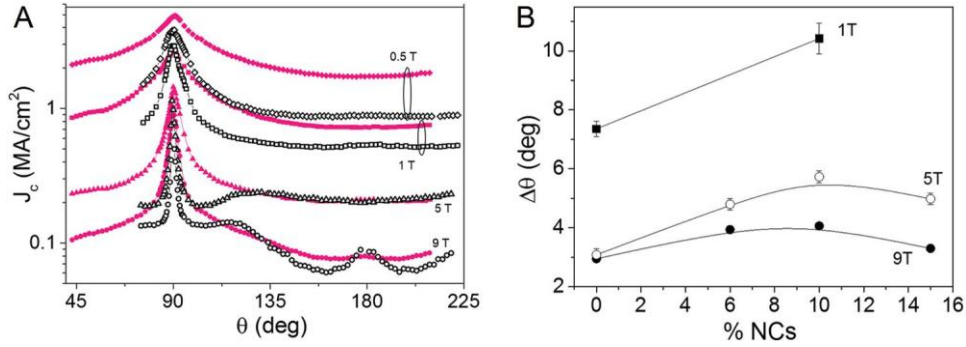

Figure 7. A) Angular dependence of the critical current density, obtained at 65 K and different magnetic fi elds, for a pristine sample (open symbols) and a nanocomposite with 10 mol% ZrO_2 (closed symbols). B) FWHM of the H//ab peak versus nanocrystal content obtained at 65 K for different magnetic fi elds.
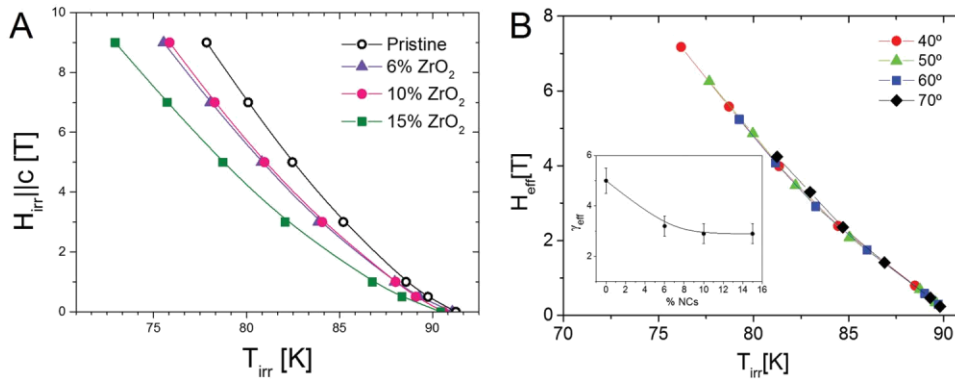

Figure 8. A) Irreversibility lines (ILs) measured for YBCO samples with different nanocrystal content and a pristine fi lm. B) Isotropic collapse of the IL curves obtained, following the Blatter scaling approach with γ_{eff} = 2.9, for the 10 mol% ZrO_2 nanocomposite. Inset shows the effective anisotropy value as a function of the nanocrystal content.

the nanocomposite with a larger NC content. A thorough analysis of the angular dependence of the IL has enabled us to determine the effective anisotropy, γ_{eff}, for these PNCs-YBCO nanocomposites and confirm that the γ_{eff} is reduced
from $\gamma_{eff} \approx 5$ to $\gamma_{eff} \approx 3$ by increasing the PNC content from 6 to 15 mol% (see Figure 8B), which is similar to the values

reported for spontaneously segregated CSD nanocomposites.[6h] This suggests that the vortex pinning properties encountered in the PNC-YBCO nanocomposites have a similar origin to the ones reported for spontaneously segregated NCs.

So, within this work, the success of this new approach was proven, although optimization of the superconducting properties at higher magnetic fields should be envisaged. For this, additional studies should be extended to lower tempera-tures (20–30 K or even 4.2 K) as this will determine the YBCO nanocomposites' possibilities for high field magnet applica-tions. We also believe that the presented approach can be opti-mized by avoiding reactivity (ZrO_2 to $BaZrO_3$) and coarsening (from 7 to 25 nm) of the preformed NCs during the thermal treatment of the YBCO layer. Reactivity should be avoided to obtain complete control over the addition of the PNCs, as oth-erwise competition between growth kinetics of the PNCs and YBCO can occur. Coarsening should be avoided, because effi-cient pinning centers should be in the range of a few nm.[5a,e] Reactivity of the preformed NCs can be avoided by using double metal oxide NCs (e.g., $BaZrO_3$). Yet, synthesis of these NCs—exhibiting the desired properties for pinning (small, agglomeration-free…)—is challenging.[19] We believe that coars-ening and even settling of the PNCs can be avoided by the use of different ligands. Although the suggested ligand (glutamine) in this paper is capable of stabilizing the PNCs in the YBCO precursor agglomeration-free with a long shelf-life, it starts to decompose at a rather low temperature, i.e., ≈185 °C. This means that this ligand will easily burn off during the pyrol-ysis treatment, causing the NCs to precipitate before the layer is solidified. So, the use of more thermally stable ligands can probably lead to better YBCO layers. However, the ligand choice is restricted. Ligands containing a high content in metals, hal-ides (except fluorine), sulfur or phosphor should be avoided, as these can otherwise negatively affect the final properties of the superconductor due to poisoning.[20] Moreover, NC sta-bilization in a highly ionic polar environment is not always straightforward.[11,12] Yet, we do believe in the potential of this new approach, using PNCs, as it offers the control over the pin-ning size and morphology, which will ultimately control the J_C.

3. Conclusion

We presented a new and successful method to incorporate pin-ning centers in a high-temperature superconductor, i.e., YBCO, through the addition of preformed nanocrystals (PNCs) using a chemical solution deposition (CSD) approach.

First, we demonstrate the stability of the synthesized ZrO_2 nanocrystals, of only 7 nm, in a TFA-YBCO precursor solu-tion. These as-synthesized nanocrystals are initially capped with long chain fatty acids, ensuring colloidal stability in nonpolar solvents. However, as the YBCO precursor typically provides a more polar environment, e.g., methanol, a ligand exchange with glutamine and trifluoroacetic anhydride was performed. Moreover, we are able to stabilize the PNCs up to 50 mol% for at least 2.5 months in a TFA-YBCO precursor solution.

Second, the PNCs' influence in the YBCO coating was studied by depositing different YBCO-PNCs suspensions on a $LaAlO_3$ substrate through spin-coating. The PNCs settle at the substrate-YBCO interface during the pyrolysis treatment, leading to an unacceptable growth of the final YBCO film and a subsequent decrease in critical current density compared to the pristine YBCO films. However, by using a pure YBCO seed layer in between the $LaAlO_3$ substrate and the PNCs-YBCO nanocomposite film, an optimal critical current density J_C of 5 MA cm^{-2} at 77 K in self-field can be obtained for a 10 mol% PNCs addition. Furthermore, a smaller magnetic field decay of J_C(H//c) and a pinning force increase by a factor 3 compared to pristine YBCO is observed opening the field for this new approach. Furthermore, a modified nanostrain distribution is found for the PNC-YBCO nanocomposite, although angular dependent critical current density and irreversibility line analysis evidence that similar vortex pinning mechanisms account for the effective increase of the superconducting proper-ties of the PNC-YBCO nanocomposites as for the self-segregated CSD nanocomposites approach previously reported. We believe even better superconducting properties can be achieved when using preformed double metal oxide nanocrystals and more thermally stable ligands stabilizing the PNCs in the YBCO precursor.

This new, successful approach of incorporation of PNCs in CSD coatings holds the promise to the effective and economi-cally efficient application of high-temperature superconductors in high magnetic field applications relevant for high field mag-nets and energy applications.

4. Experimental Section

Nanocrystal Synthesis: ZrO_2 NCs are synthesized according to a microwave-assisted solvothermal treatment.[10,11a] The ZrO_2 NCs are synthesized using zirconium chloride (0.59 mmol), dibenzyl ether (0.5 mL), and benzyl alcohol (4 mL) as solvent. After a microwave-assisted solvothermal treatment at 220 °C for 4 h, a stable colloidal dispersion of the NCs capped with dodecanoic acid (0.2 mmol) is obtained in chloroform (4 mL) through the aid of oleyl amine (0.15 mmol). To achieve a stable NC dispersion in methanol, a ligand exchange is performed.[12] First, the dodecanoic acid-stabilized NCs (1 mL) are precipitated with acetone and subsequently glutamine (0.05 mmol), dissolved in 1 mL dry methanol, is added together with trifluoroacetic anhydride (0.4 mmol). An ultrasonic treatment of ≈30 min results in a clear and colorless dispersion. The NCs suspension is purifi ed by a precipitation–dissolution process using toluene (1:3 volume) to precipitate the NCs, and dry methanol to redisperse the purifi ed NCs. If the dispersion does not become completely transparent, an excess of trifluoroacetic anhydride should be used.

Layer Formation: YBCO-ZrO_2 precursor solutions are prepared by introducing the ZrO_2 NCs in different mol% to a TFA-YBCO precursor solution. The preparation of the TFA-YBCO precursor solution is described elsewhere.[3b] Mol% of 0, 1, 3, 6, 10, and 15% have been investigated. The YBCO-NCs precursor fi lms are prepared by depositing the precursors on 5 × 5 mm $LaAlO_3$ (LAO) single crystal substrates via spin coating (6000 rpm–2 min). These deposited layers are thermally treated for pyrolysis and subsequent crystallization to convert the layers into the fi nal YBCO nanocomposite thin fi lms.[3] Generally, the pyrolysis treatment was performed in a tubular furnace under a humid oxygen gas flow at 310 °C for 30 min. The crystallization treatment was performed at 810 °C for 180 min in a wet N_2 atmosphere with an O_2 partial pressure of 200 ppm. Finally, the superconducting YBCO phase was obtained by oxygen annealing at 450 °C for 210 min. To start from a LAO substrate with an interfacial pure YBCO seed layer, fi rst a 0.375 M total metal concentration of TFA-YBCO precursor is deposited on the LAO substrate and spin-coated. This layer is pyrolyzed, without a dwell of 30 min, before the NCs-YBCO suspension is deposited on top. Directly afterward, the bilayer is crystallized using the thermal treatment previously mentioned.

Nanocrystal Characterization: The metal oxide NCs were characterized via TEM using a JEOL model JEM-2200FS, XRD using a Thermo Scientifi c ARL X'tra X-ray diffractometer with the Cu K_α line as primary X-ray source, and DLS measurements using a Malvern Nano ZS in backscattering mode (173°).

Layer Characterization: The microstructure and phase analysis of the fully converted YBCO nanocomposite fi lms was performed by 2D X-ray diffraction using a Bruker AXS GADDS diffractometer. The nanocrystal size, distribution, chemical composition, and atomic scale defects of the PNCs in the fi nal nanocomposite layer were investigated by LAADF-STEM and HAADF-STEM and EDX studies using a FEI Titan "cubed" electron microscope, equipped with an aberration corrector for the probe-forming lens as well as a high-brightness gun and a "Super-X" wide solid angle EDX detector. The electron microscope was operated at 200 kV. XPS measurements were recorded on an X-ray photoelectron spectroscopy S-Probe XPS spectrometer with monochromated Al (1486 eV) exciting radiation from Surface Science Instruments (VG). The flood gun was set at 3 eV. A nickel grid was placed 3 mm above the samples in order to suppress charging of the samples. The samples were attached to the stage using conducting C-tape, a shortcut between the top of the sample and the stage was prepared with Cu-tape. Experimental data were processed using the software package CasaXPS (Casa Software Ltd., UK), using Shirley background subtraction. Sputtering of an area of 3 × 3 mm^2 for 500 s/800 s was performed with an Ar^+ ion gun (4 keV). After each consecutive sputter cycle an area of 250 × 1000 μm^2 was analyzed. Regions for C 1s, Y 3d, Zr 3p-3p1/2, La 4p1/2, La 3d5/2, and O 1s peaks were acquired. Angular transport I(V) characteristics and resistivity measurements were carried out in a PPMS Quantum

Design system provided with a 9 T magnet and variable temperature from 5 to 300 K, to determine superconducting transition temperature T_c and the critical current density $J_C(T, H, \vartheta)$. Narrow bridges of 200 μm lengths and 10 to 30 μm width were fabricated with standard photolithography with a Durham Magneto Optics Std MicroWriter. Silver metal contacts were evaporated and post-annealed, ensuring contact resistances below 10 μΩ. Samples were measured with the standard four-probe method. The applied current was sent parallel to the *ab*-planes and J_C was determined by using a 10 μV cm^{-1} criterion, taking into account the fi lm thickness of 180 nm. The transition width T is determined via a 10%–90% criteria of the resistivity versus temperature curve. The irreversibility line $H_{irr}(T, \vartheta)$ is determined from the resistivity curves as a function of temperature for different applied magnetic fi elds using a criteria of $\rho/\rho_{300\ K} = 10^{-3}$. In angular measurements, the magnetic fi eld was rotated from the *c*-axis ($\vartheta = 180°$) to the *ab*-plane ($\vartheta = 90°$), ensuring the maximum Lorentz force confi guration.

Acknowledgements

References:

[1]a) D. Larbalestier, A. Gurevich, D. M. Feldmann, A. Polyanskii, *Nature* **2001**, *414*, 368; b) V. Selvamanickam, Y. Chen, X. Xiong,
Y. Xie, X. Zhang, A. Rar, M. Martchevskii, R. Schmidt, K. Lenseth,
J. Herrin, *Phys. C* **2008**, *468*, 1504; c) A. P. Malozemoff, in *Annual Review of Materials Research*, Vol. *42* (Ed: D. R. Clarke), Annual Reviews, Palo Alto, CA **2012**, p. 373; d) Y. Shiohara, T. Taneda,
M. Yoshizumi, *Jpn. J. Appl. Phys.* **2012**, *51*, 010007.

[2]a) T. Araki, I. Hirabayashi, *Supercond. Sci. Technol.* **2003**, *16*, R71; b) X. Obradors, T. Puig, S. Ricart, M. Coll, J. Gazquez, A. Palau,
X. Granados, *Supercond. Sci. Technol.* **2012**, *25*, 123001; c) I. Van Driessche, J. Feys, S. C. Hopkins, P. Lommens, X. Granados,
B. A. Glowacki, S. Ricart, B. Holzapfel, M. Vilardell, A. Kirchner,
M. Backer, *Supercond. Sci. Technol.* **2012**, *25*, 065017.

[3]A. Llordes, K. Zalamova, S. Ricart, A. Palau, A. Pomar, T. Puig,
A. Hardy, M. K. Van Bael, X. Obradors, *Chem. Mater.* **2010**, *22*, 1686.

[4]X. Obradors, T. Puig, A. Palau, A. Pomar, F. Sandiumenge, P. Mele, Matsumoto, *Comprehensive Nanoscience and Technology*, Academic Press, Amsterdam **2011**.

[5]
X. Obradors, *Nat. Mater.* **2007**, *6*, 367; b) T. G. Holesinger, L. Civale,
B. Maiorov, D. M. Feldmann, J. Y. Coulter, J. Miller, V. A. Maroni,
Z. J. Chen, D. C. Larbalestier, R. Feenstra, X. P. Li, M. B. Huang,
T. Kodenkandath, W. Zhang, M. W. Rupich, A. P. Malozemoff, *Adv. Mater.* **2008**, *20*, 391; c) S. Kang, A. Goyal, J. Li, A. A. Gapud,
P. M. Martin, L. Heatherly, J. R. Thompson, D. K. Christen,

F. A. List, M. Paranthaman, D. F. Lee, *Science* **2006**, *311*, 1911; d) J. L. Macmanus-Driscoll, S. R. Foltyn, Q. X. Jia, H. Wang,

A. Serquis, L. Civale, B. Maiorov, M. E. Hawley, M. P. Maley,

D. E. Peterson, *Nat. Mater.* **2004**, *3*, 439; e) K. Matsumoto, P. Mele, *Supercond. Sci. Technol.* **2010**, *23*, 014001; f) A. Xu, L. Delgado,

N. Khatri, Y. Liu, V. Selvamanickam, D. Abraimov, J. Jaroszynski,

F. Kametani, D. C. Larbalestier, *APL Mater.* **2014**, *2*, 046111.

[6] a) M. Coll, R. Guzman, P. Garces, J. Gazquez, V. Rouco, A. Palau,

S. Ye, C. Magen, H. Suo, H. Castro, T. Puig, X. Obradors, *Supercond. Sci. Technol.* **2014**, *27*, 044008; b) F. Z. Ding, H. W. Gu,

T. Zhang, H. Y. Wang, F. Qu, X. Y. Peng, W. W. Zhou, *Acta Phys. Sin.*

2013, *62*, 137401; c) F. Z. Ding, H. W. Gu, T. Zhang, H. Y. Wang, F. Qu, Q. Q. Qiu, S. T. Dai, X. Y. Peng, *Chin. Phys. B* **2013**, *22*, 077401; d) F. Z. Ding, H. W. Gu, T. Zhang, H. Y. Wang, F. Qu,

A. Q. Qiu, S. T. Dai, X. Y. Peng, J. L. Cao, *Appl. Surf. Sci.* **2014**, *314*, 622; e) L. H. Jin, S. N. Zhang, Z. M. Yu, C. S. Li, J. Q. Feng, Sulpice, Y. Wang, P. X. Zhang, *Mater. Chem. Phys.* **2015**,

149, 188; f) F. Martinez-Julian, S. Ricart, A. Pomar, M. Coll, P. Abelian, F. Sandiumenge, M. J. Casanove, X. Obradors, T. Puig, Pastoriza-Santos, L. M. Liz-Marzan, *J. Nanosci. Nanotechnol.* **2011**, *11*, 3245; g) T. Petrisor, R. B. Mos, M. Nasui, M. S. Gabor,

A. Augieri, G. Celentano, D. De Felkis, E. Bemporad, L. Ciontea,

J. Supercond. Nov. Magn. **2014**, *27*, 2439; h) A. Llordes, A. Palau,

J. Gazquez, M. Coll, R. Vlad, A. Pomar, J. Arbiol, R. Guzman,

S. Ye, V. Rouco, F. Sandiumenge, S. Ricart, T. Puig, M. Varela,

D. Chateigner, J. Vanacken, J. Gutierrez, V. Moshchalkov,

G. Deutscher, C. Magen, X. Obradors, *Nat. Mater.* **2012**, *11*, 329.

[7] a) M. Baghbanzadeh, L. Carbone, P. D. Cozzoli, C. O. Kappe, *Angew. Chem. Int. Ed.* **2011**, *50*, 11312; b) Y. W. Jun, J. S. Choi, J. Cheon, *Angew. Chem. Int. Ed.* **2006**, *45*, 3414; c) J. Lee, S. Zhang, S. H. Sun, *Chem. Mater.* **2013**, *25*, 1293; d) J. Park, J. Joo, S. G. Kwon, Y. Jang,

T. Hyeon, *Angew. Chem. Int. Ed.* **2007**, *46*, 4630; e) N. Pinna,

M. Niederberger, *Angew. Chem. Int. Ed.* **2008**, *47*, 5292; f) S. Shi, J.-Y. Hwang, *J. Miner. Mater. Charact. Eng.* **2003**, *2*, 101.

[8] a) I. Bretos, T. Schneller, M. Falter, M. Backer, E. Hollmann, R. Wordenweber, L. Molina-Luna, G. Van Tendeloo, O. Eibl, *J. Mater. Chem. C* **2015**, *3*, 3971; b) P. Cayado, K. De Keukeleere, A. Garzon, L. Perez-Mirabet, A. Meledin, J. De Roo, F. Valles, B. Mundet,

H. Rijckaert, G. Pollefeyt, M. Coll, S. Ricart, A. Palau, J. Gazquez,

J. Ros, G. Van Tendeloo, I. Van Driessche, T. Puig, X. Obradors,

Supercond. Sci. Technol. **2015**, *28*, 124007.

[9] A. Palau, T. Puig, X. Obradors, E. Pardo, C. Navau, A. Sanchez,

A. Usoskin, H. C. Freyhardt, L. Fernandez, B. Holzapfel, R. Feenstra,

Appl. Phys. Lett. **2004**, *84*, 230.

[10] K. De Keukeleere, J. De Roo, P. Lommens, J. C. Martins,

P. Van der Voort, I. Van Driessche, *Inorg. Chem.* **2015**, *54*, 3469.

[11] a) J. De Roo, F. Van den Broeck, K. De Keukeleere, J. C. Martins,

I. Van Driessche, Z. Hens, *J. Am. Chem. Soc.* **2014**, *136*, 9650;

b) J. De Roo, Y. Justo, K. De Keukeleere, F. Van den Broeck,

J. C. Martins, I. Van Driessche, Z. Hens, *Angew. Chem. Int. Ed.* **2015**, *54*, 6488; c) I. Moreels, Y. Justo, B. De Geyter, K. Haustraete,

J. C. Martins, Z. Hens, *ACS Nano* **2011**, *5*, 2004; d) B. Fritzinger,

R. K. Capek, K. Lambert, J. C. Martins, Z. Hens, *J. Am. Chem. Soc.* **2010**, *132*, 10195.

[12]   J. De Roo, S. Coucke, H. Rijckaert, K. De Keukeleere, D. Sinnaeve,

Z. Hens, J. C. Martins, I. Van Driessche, *Langmuir* **2016**, *32*, 1962.

[13]   a) X. Obradors, T. Puig, A. Pomar, F. Sandiumenge, N. Mestres,

M. Coll, A. Cavallaro, N. Roma, J. Gazquez, J. C. Gonzalez,

O. Castano, J. Gutierrez, A. Palau, K. Zalamova, S. Morlens,

A. Hassini, M. Gibert, S. Ricart, J. M. Moreto, S. Pinol, D. Isfort,

J. Bock, *Supercond. Sci. Technol.* **2006**, *19*, S13; b) M. Yoshizumi,

T. Nakanishi, J.   Matsuda, K. Nakaoka, Y.   Sutoh, T.   Izumi,

Y.   Shiohara, *Phys. C* **2008**, *468*, 1531.

[14]   a) Z. H. Gu, W. T. Wang, C. Y. Bai, Y. Q. Guo, Y. M. Lu, Z. Y. Liu,

Q. Lu, G. Q. Shu, C. B. Cai, *Chin. Phys. B* **2015**, *24*, 6; b) X. Obradors,

T. Puig, M. Gibert, A. Queralto, J. Zabaleta, N. Mestres, *Chem. Soc. Rev.* **2014**, *43*, 2200.

[15]   M. Coll, R. Guzman, P. Garces, J. Gazquez, V. Rouco, A. Palau,

S. Ye, C. Magen, H. Suo, H. Castro, T. Puig, X. Obradors, *Supercond. Sci. Technol.* **2014**, *27*, 044008.

[16]   A. Palau, A. Llordes, M. Gibert, T. Puig, A. Pomar, X. Obradors,

IEEE Trans. Appl. Supercond. **2011**, *21*, 3243.

[17]   A. Palau, E. Bartolome, A. Llordes, T. Puig, X. Obradors, *Supercond. Sci. Technol.* **2011**, *24*, 125010.

[18]   a) R. Guzman, J. Gazquez, V. Rouco, A. Palau, C. Magen, M. Varela,

J. Arbiol, X. Obradors, T. Puig, *Appl. Phys. Lett.* **2013**, *102*, 081906; b) V. Rouco, A. Palau, R. Guzman, J. Gazquez, M. Coll, X. Obradors,

T. Puig, *Supercond. Sci. Technol.* **2014**, *27*, 125009.

[19]   a) A. Aimable, B. Xin, N. Millot, D. Aymes, *J. Solid State Chem.* **2008**, *181*, 183; b) L. R. Macario, M. L. Moreira, J. Andres, E. Longo, *CrystEngComm* **2010**, *12*, 3612; c) M. Niederberger, G. Garnweitner,

N. Pinna, M. Antonietti, *J. Am. Chem. Soc.* **2004**, *126*, 9120.

[20]   S. R. Foltyn, L. Civale, J. L. Macmanus-Driscoll, Q. X. Jia, B. Maiorov,

H. Wang, M. Maley, *Nat. Mater.* **2007**, *6*, 631.

Supporting Information

Superconducting YBa$_2$Cu$_3$O$_{7-\delta}$ Nanocomposites Using Preformed ZrO$_2$ Nanocrystals: Growth Mechanisms and Vortex Pinning Properties

Katrien De Keukeleere◊, Pablo Cayado◊, Alexander Meledin, Ferran Vallès, Jonathan De Roo, Hannes Rijckaert, Glenn Pollefeyt, Els Bruneel, Anna Palau, Mariona Coll, Susagna Ricart, Gustaaf Van Tendeloo, Teresa Puig, Xavier Obradors and Isabel Van Driessche
◊both authors contributed equally to this work

1. NCs incorporated in TFA-YBCO: molar percentage

To calculate the NCs amount that will be present in the final YBCO layer, the concentration of both should be known. In general, we start from a 1.5 M TFA-YBCO precursor solution (total metal concentration), while the NCs' concentration is determined after ligand exchange

through gravimetrical analysis (approximately 0.08 M). The molar percentage (mol-%) of NCs in TFA-YBCO is determined with respect to the yttrium ion concentration. Finally, the suspension is diluted until a total metal concentration of 0.75M of YBCO is obtained, before spin-coating.

The suspensions remain stable for at least 2.5 months, while some agglomeration starts to occur after 4 months for the 50 mol-% NCs-YBCO suspensions (Figure S 1).
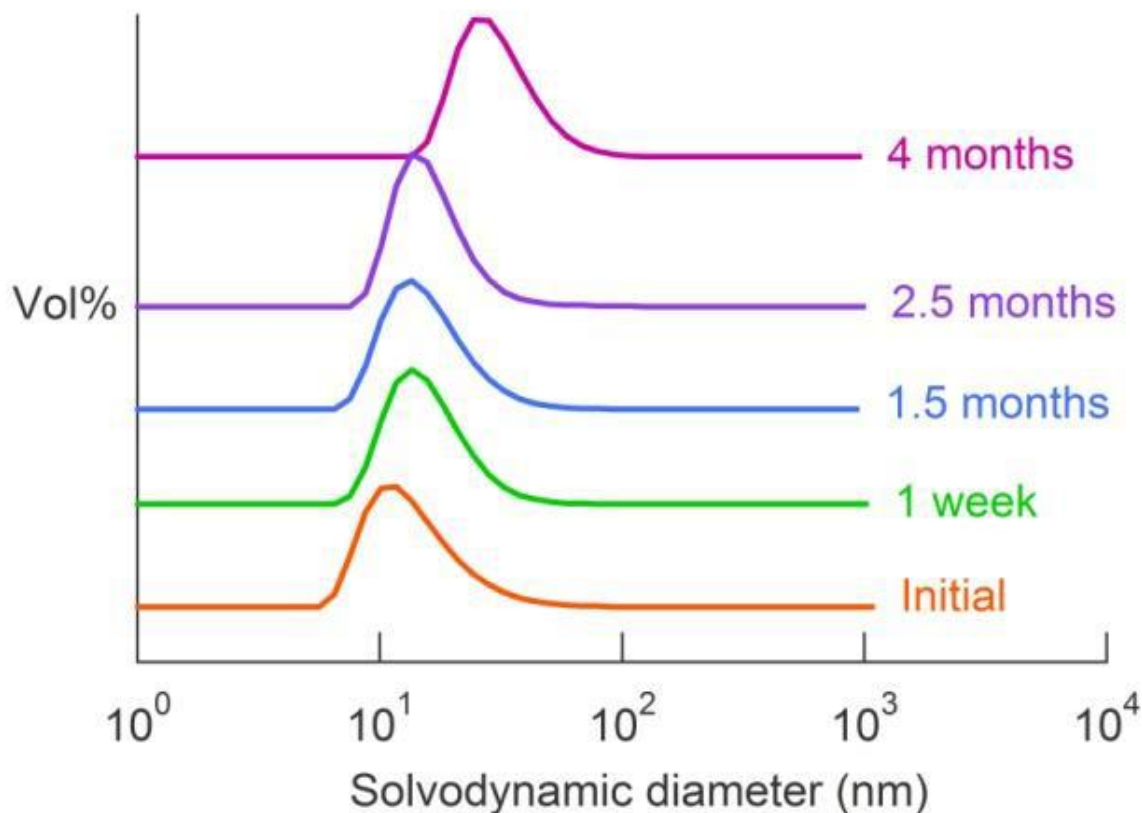

Figure S 1. DLS analysis on a 50 mol-% ZrO_2 NC - TFA-YBCO suspension over time.

2. 2D XRD diffractograms of 0, 1, 3 and 10 mol-% ZrO_2 NC – YBCO film without seed layer

The *(00l)* YBCO reflections in the XRD diffractograms indicate *c*-axis orientation, while the presence of the *(103)* YBCO reflection shows random growth (Figure S 2). At high loadings (e.g. 10 mol-% ZrO_2), the *(00l)* reflections are present as rings in the 2D X-ray diffraction pattern, indicating that actually polycrystalline YBCO is formed instead of purely *c*-axis oriented *(00l)* YBCO. The presence of the 2θ reflection at 43° of *(200)* $BaZrO_3$, suggest the transformation of ZrO_2 into $BaZrO_3$ NCs as the ZrO_2 2θ reflections remain absent.
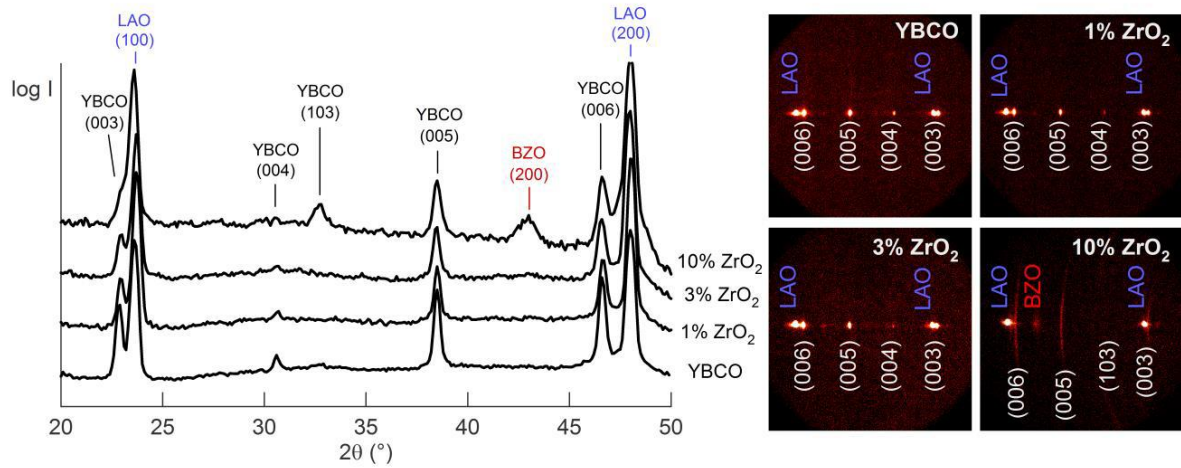
Figure S 2. (2D-)XRD diffractograms of YBCO films with 0, 1, 3 and 10 mol-% of preformed ZrO_2 NCs on a LAO.

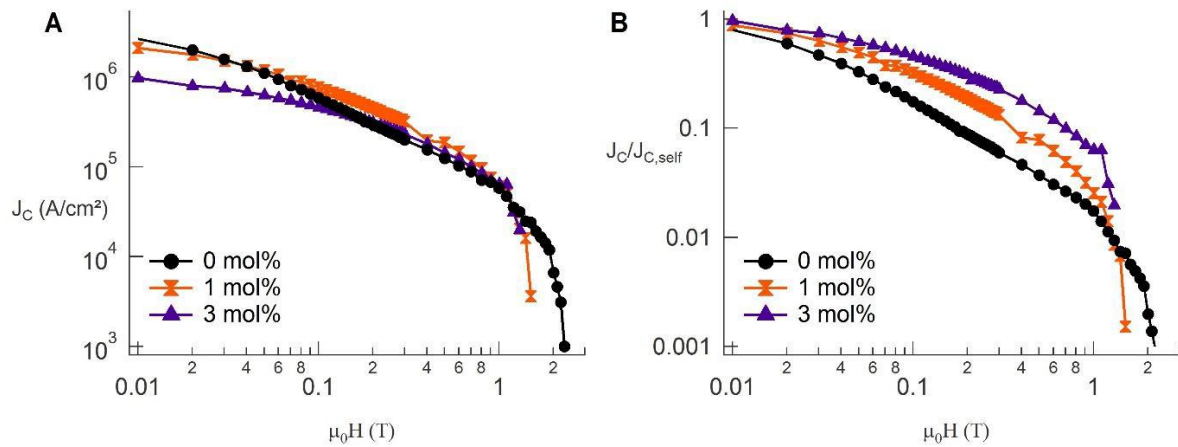# 3. Physical properties of 0, 1, 3 and 10 mol-% ZrO_2 NC – YBCO film without seed layer

Figure S 3. (A) Magnetic field dependence of the critical current density at 77 K and H // c and (B) normalized to self-field value for YBCO na nocomposites with different mol-% of preformed ZrO_2 NCs deposited on a LAO
substrate.

Table S 1. Physical properties of the 0, 1, and 3 mol-% preformed ZrO_2 NCs – YBCO films on a LAO substrate

# [mol-%] ZrO_2	J_C (77K) [MA/cm²]	T_C [K]	ΔT [K]
0	3.35	89.6	4.5
1	2.39	89.4	5.4
3	1	89	9.7

4. HAADF-STEM, EDX and HR-TEM analysis on the 3 mol-% ZrO_2 – YBCO nanocomposite

The majority of the Zr-phase, or formed $BaZrO_3$ NCs, is present at the interface of the LAO substrate and the YBCO layer (Figure S 4 A, B and C). The NCs in the YBCO layer are grown from the initial 7 nm ZrO_2 NCs to 15 nm if $BaZrO_3$ NCs (Figure S 4 D), which is not only due to transformation of ZrO_2 to $BaZrO_3$, but also due to the occurrence of agglomeration of a few ZrO_2 NCs before the transformation.
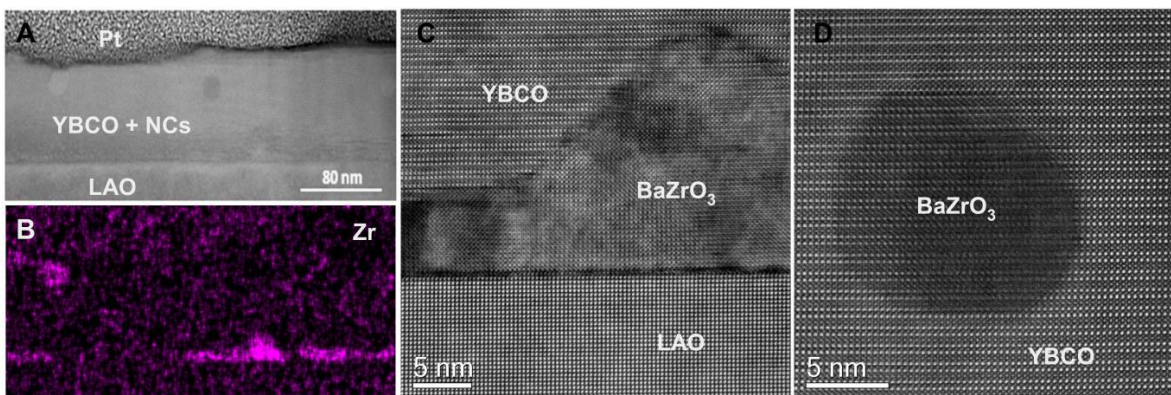

Figure S 4. (A) HAADF – STEM and (B) EDX image on the 3 mol-% preformed NCs - YBCO nanocomposite indicating the presence of Zr in the layer. High-resolution Z-contrast image of the same nanocomposite showing local microstructures of $BaZrO_3$ NCs (C) nucleated on the LAO substrate and (D) randomly oriented within the epitaxial YBCO matrix.

5. Centrifugation experiment & XPS analysis on the 10 mol-% ZrO_2 – YBCO nanocomposite

Spin coating is used as deposition method, in which centrifugal and centripetal forces are present during deposition. These forces can coerce the NCs the substrate, resulting in settling of the PNCs at the substrate in the final nanocomposite layer. To gain an idea, if the used deposition method, spin coating, lies at the basis of this problem, a centrifugation experiment 5

was performed on a 10 mol-% ZrO_2 NC-YBCO precursor suspension. According to the DLS analysis (Figure S 5), the solvodynamic diameter and the Z-average, indicating the presence of agglomeration in a suspension, does not change. Hence, the precursor suspension was not affected by centrifugation, indicating that the NCs should remain individual in the deposited layer before the pyrolysis treatment.
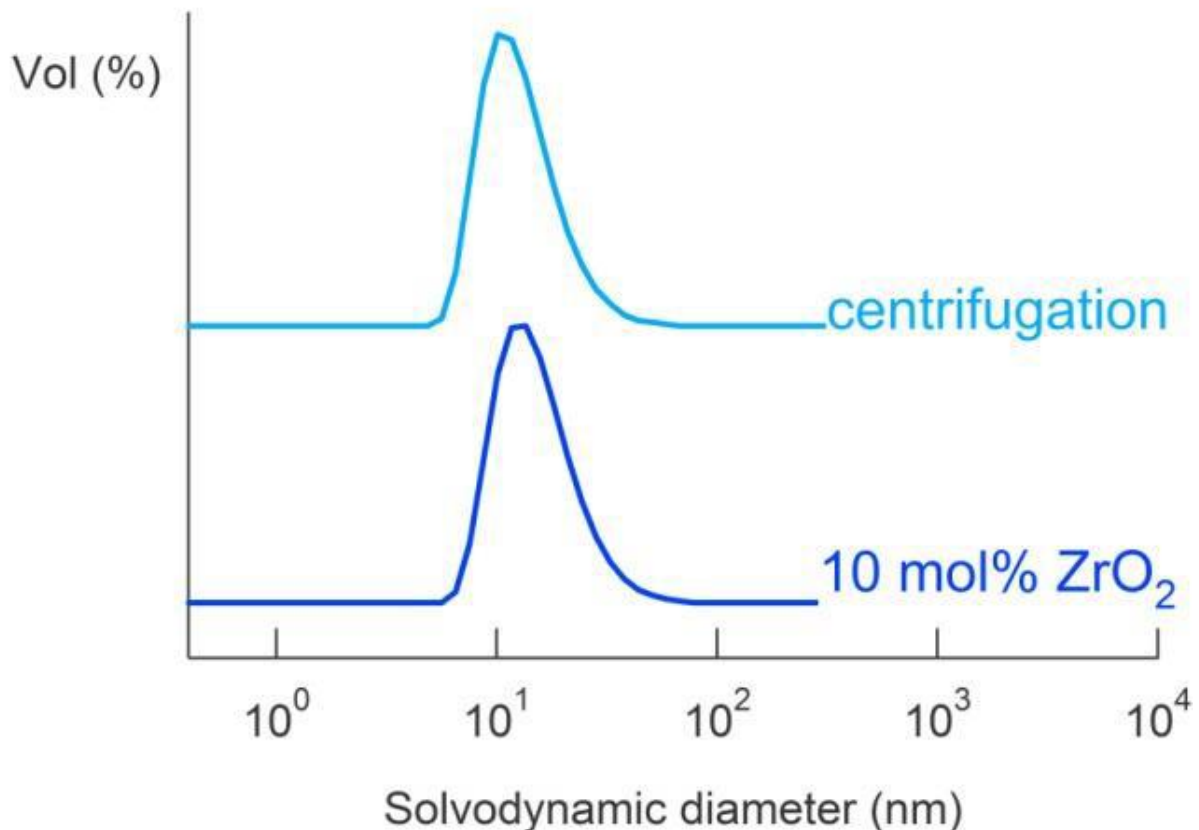
Figure S 5. DLS analysis on a 10 mol-% ZrO_2 NC-YBCO precursor suspension before and after centrifugation, indicating a solvodynamic diameter of approximately 11.5 nm.

To determine if the ZrO_2 PNCs settle on the substrate, during pyrolysis or crystallization, sputtering and subsequent XPS analysis was performed on a pyrolyzed and crystallized layer. Figure S 6 A and B shows the relative composition of Y, Zr and La in a 10 mol-% preformed ZrO_2 NC – YBCO layer, indicating the presence of Zr throughout the layer after the pyrolysis and crystallization treatment. The dotted lines indicate the transition of the YBCO nanocomposite (1) to the LAO substrate (2). The measured Zr seems to be present in the LAO
substrate after the crystallization treatment, which can be due to diffusion of Zr, but also due to mixing of the sample while sputtering. The XPS data reveals that Zr is present throughout the YBCO film, but the distribution is not homogeneous, namely a rise in Zr signal arises at the interface of LAO and YBCO both after the pyrolysis and crystallization treatment. This means that the preformed ZrO_2 NCs settle down on the substrate during the pyrolysis treatment.
By using an YBCO seed layer in between the LAO substrate and the YBCO nanocomposite, the properties are drastically improved. Again XPS analysis was performed after pyrolysis
6
and crystallization treatment to determine the presence of Zr throughout the layer (Figure S 6 C and D). The dotted lines indicate the transition of the YBCO nanocomposite (1) to the LAO

substrate (2), with in between the pure YBCO seed layer (3). It is immediately noticeable that the Zr phase is more homogeneously distributed throughout the YBCO layer. Some Zr accumulation seem to be present at the YBCO seed layer after pyrolysis, which disappears after the crystallization treatment. Hence, the addition of a seed layer seems to have a beneficial effect on the Zr distribution throughout the superconducting layer.
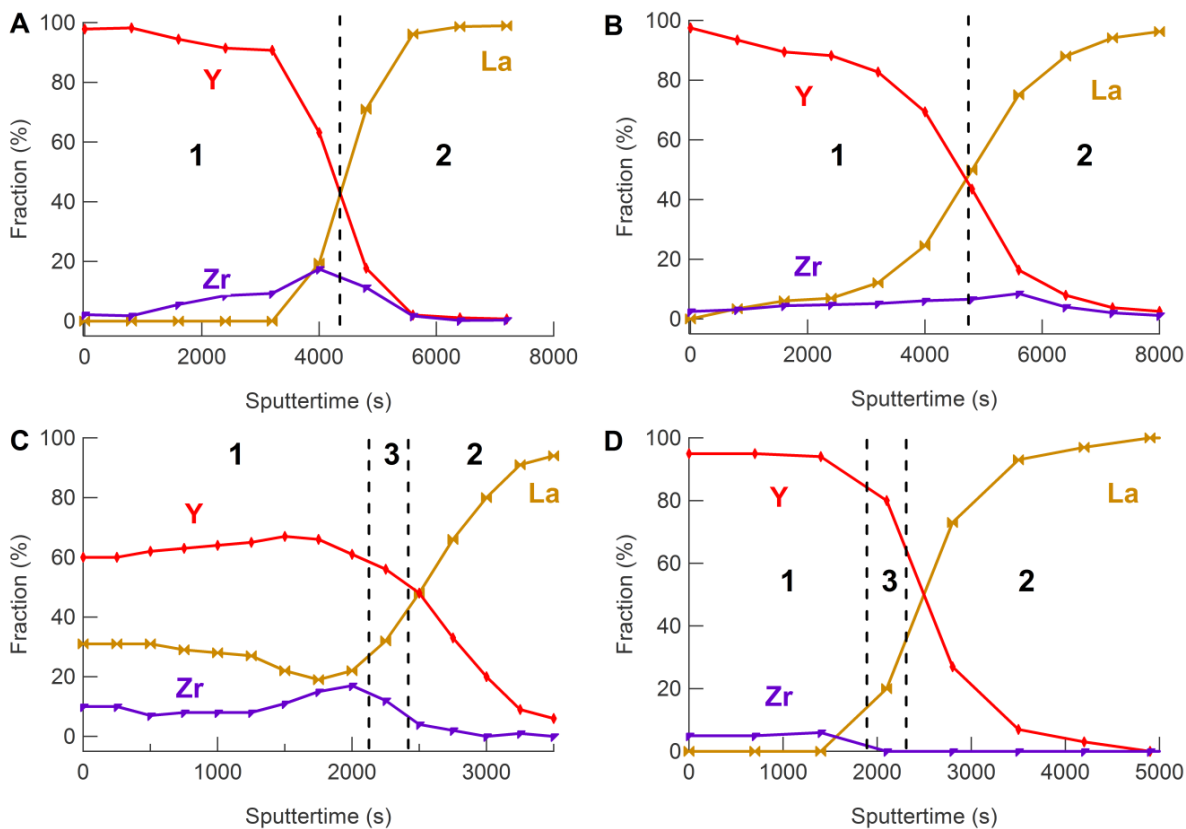

Figure S 6. Relative composition of Y, Zr and La in a 10 mol-% preformed ZrO_2 NC – YBCO film deposited on a LAO substrate after (A) pyrolysis and (B) crystallization. Relative composition of Y, Zr and La in a 15 mol-% preformed ZrO_2 NC – YBCO film deposited on an YBCO seed layer and LAO substrate after (C) pyrolysis and (D) crystallization. Both determined from XPS analysis.

6. Quench experiments

Two quench experiments were performed at 790 °C or 760 °C, using the same concentration of ZrO_2 NCs, i.e., a pyrolyzed 10 mol-% ZrO_2 NC – YBCO layer directly deposited on a LAO substrate. The pyrolysed sample is subjected to a standard crystallization program (0.6 L min-1 of N_2 with 200 ppm of O_2 in humid atmosphere and a heating ramp of 25 °C min-1). At the desired quench temperature (790 °C or 760 °C), the sample is immediately removed from the furnace into the air and placed on a cold metal surface (between 10 – 15 °C) to freeze the sample at this stage. The quenched samples are analyzed via XRD measurements, indicated in Figure S 7. Both quench experiments display reflections of CuO, $Y_2Cu_2O_5$ and BaF_2, the precursor of YBCO. Also $BaZrO_3$ (BZO) reflections are present in both experiments. However, the quenched sample at 790 °C shows narrowing of the CuO reflections and sometraces of *(00l)* YBCO reflections appear, indicating the formation of c-axis oriented YBCO.

Hence, BZO nucleates before YBCO formation. It can also be noted that the quenched sample at 790 °C also exhibits the (103) YBCO reflection, which is probably formed during thecooling process in air.
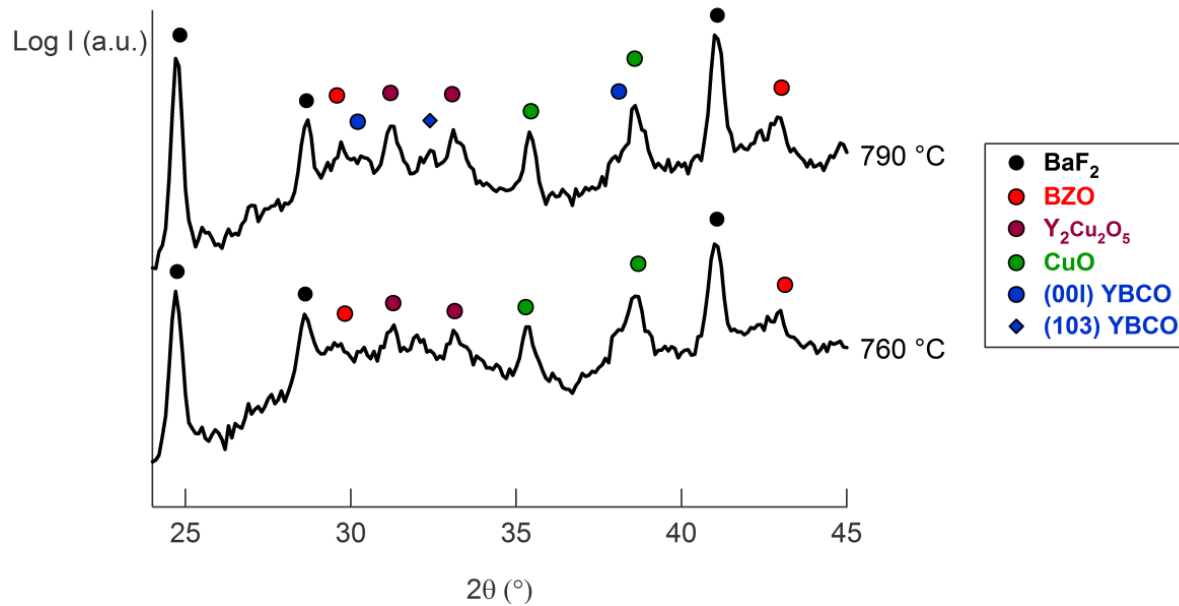

Figure S 7. XRD diffractograms of 10 mol-% ZrO$_2$ PNC - YBCO films after a quench experiment at 760 °C and
790 °C temperatures.